

RESEARCH ARTICLE

10.1029/2017JB015338

Key Points:

- This study presents the evolution of frictional stability-permeability in sheared smooth natural and sintered fractures with distinct mineral compositions
- Frictional stability increases with carbonate and clay content and decreases with tectosilicate content
- Permeability evolution is inversely correlated with frictional stability

Correspondence to:

Y. Fang,
yi.fang@utexas.edu

Citation:

Fang, Y., Elsworth, D., Wang, C., & Jia, Y. (2018). Mineralogical controls on frictional strength, stability, and shear permeability evolution of fractures. *Journal of Geophysical Research: Solid Earth*, 123, 3549–3563. <https://doi.org/10.1029/2017JB015338>

Received 12 DEC 2017

Accepted 26 APR 2018

Accepted article online 4 MAY 2018

Published online 19 MAY 2018

Mineralogical Controls on Frictional Strength, Stability, and Shear Permeability Evolution of Fractures

Yi Fang^{1,2}, Derek Elsworth^{2,3}, Chaoyi Wang², and Yunzhong Jia^{2,4}

¹Institute for Geophysics, Jackson School of Geosciences, University of Texas at Austin, Austin, TX, USA, ²Department of Energy and Mineral Engineering, EMS Energy Institute, and G3 Center, Pennsylvania State University, University Park, PA, USA, ³Department of Geosciences, EMS Energy Institute, and G3 Center, Pennsylvania State University, University Park, PA, USA, ⁴State Key Laboratory for Coal Mine Disaster Dynamics and Control, Chongqing University, Chongqing, China

Abstract Massive fluid injection into the subsurface can induce microearthquakes by reactivating preexisting faults or fractures as seismic or aseismic slip. Such seismic or aseismic shear deformations may result in different modes of permeability evolution. Previous experimental studies have explored frictional stability-permeability relationships of carbonate-rich and phyllosilicate-rich samples under shear, suggesting that friction-permeability relationship may be primarily controlled by fracture minerals. We examine this relationship and identify the role of mineralogy (i.e., tectosilicate, carbonate, and phyllosilicate content) using direct-shear experiments on smooth saw-cut fractures of natural rocks and sintered fractures with distinct mineralogical compositions. These results indicate that the friction-permeability relationship is controlled by mineralogy. Frictional strength and permeability change upon reactivation decrease with phyllosilicate content but increase with tectosilicate content. In contrast, the reverse trend is observed for frictional stability (*a-b*). However, the permeability change decreases with carbonate content while both frictional strength and stability increase. The permeability change always decreases with an increase in frictional stability. This relationship implies a new mechanical-hydro-chemical coupling loop via a linkage of frictional properties, mineralogy, and permeability.

1. Introduction

Subsurface engineering activities, such as the development of enhanced geothermal systems, stimulation of shale gas reservoirs, and the long-term geological sequestration of CO₂, all involve massive fluid injections. The injected fluids can reduce the effective normal stress on preexisting faults and fractures and induce microearthquakes in the form of seismic slip, slow slip, and aseismic slip (Cornet et al., 1997; Fang et al., 2016; Guglielmi, Cappa, et al., 2015; Zoback et al., 2012). Some in situ experiments suggest that these shear deformations may affect the transport characteristics of the reservoir formation. For instance, locally elevated permeabilities at seismogenic depths are observed in Integrated Ocean Drilling Program drill holes on the Cascadia margin (Davis et al., 1995). Permeability enhancement is observed in the reactivation of faults in both Tournemire shale and carbonates and is associated to dilatant slip (Guglielmi, Elsworth, et al., 2015; Guglielmi, Cappa, et al., 2015). Laboratory observations indicate that permeability may enhance due to significant shear dilation or decrease as a result of progressive formation of gouge during shear slip (Barton et al., 1985; Faoro et al., 2009; Im et al., 2018; Rutter & Mecklenburgh, 2017). These concurrent observations of fault slip and fluid flow pose a ubiquitous question in understanding fault permeability evolution in response to fault movement. This further provides significant insight of fluid trapping by sealing layers, migration of hydrocarbons within fractures, and degradation or enhancement of integrity of seal systems. Theoretical treatments and experimental results suggest that fault reactivation depends on the strength of the fault (Ben-David et al., 2010; Kilgore et al., 2012; Marone, 1995) and the nucleation of instability is governed by the frictional behavior within the fault associated with slip velocity perturbations (Brune, 1970; Ikari et al., 2011; Johnson & Scholz, 1976). This frictional behavior is empirically defined under the frame of rate-and-state friction theory (Dieterich, 1978, 1979; Ruina, 1983), in which the friction coefficient μ (also known as the frictional strength) is written as

$$\mu = \mu_0 + a \cdot \ln\left(\frac{V}{V_0}\right) + b \cdot \ln\left(\frac{V_0 \theta}{D_c}\right) \quad (1)$$

$$\frac{d\theta}{dt} = 1 - \frac{V\theta}{D_c} \quad (2)$$

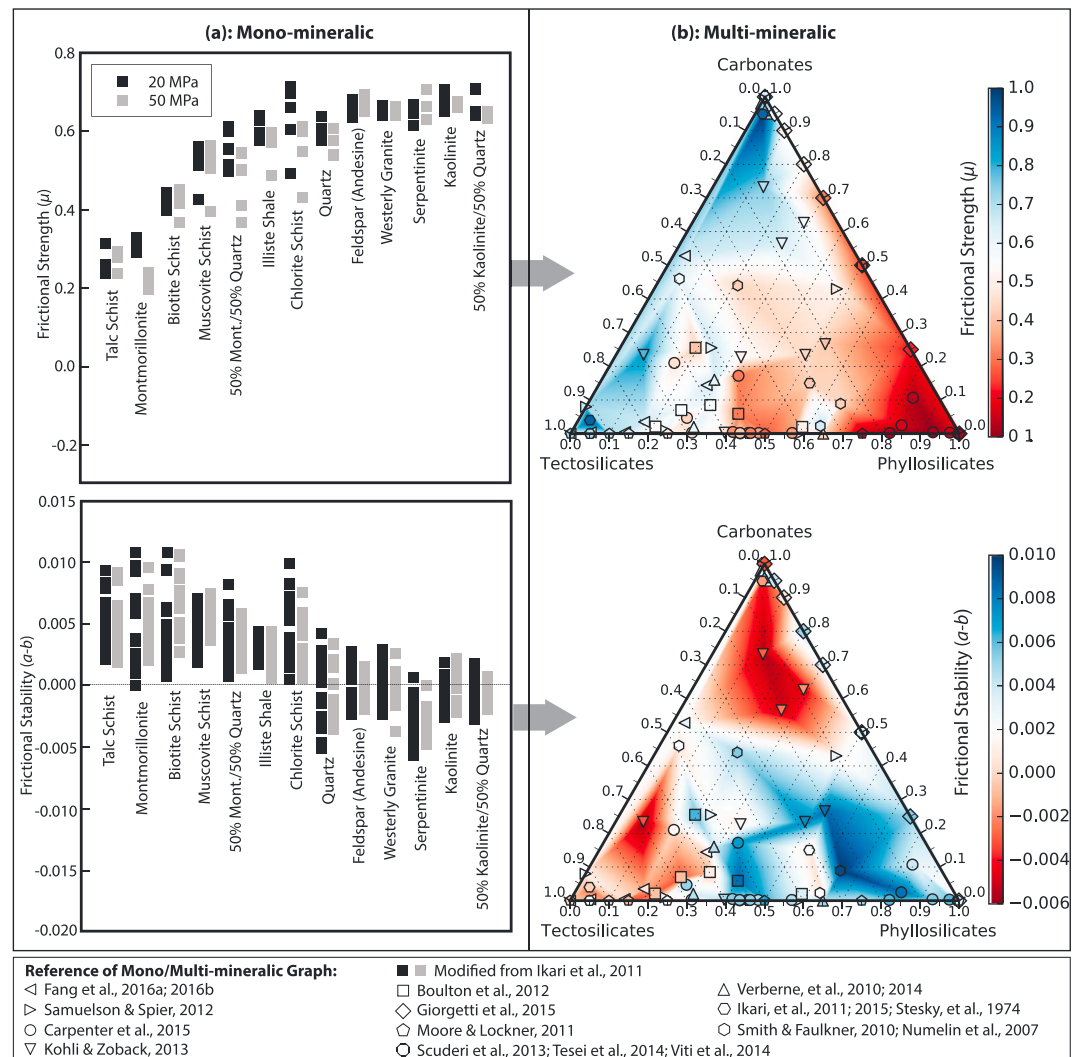


Figure 1. (a) Frictional strength μ and stability ($a-b$) of mono-mineralogical samples. (b) Frictional strength μ and stability ($a-b$) of samples with varied proportions of carbonate-tectosilicate-phyllsilicate mixtures. Source data of this ternary graph are listed in Table 1.

where μ_0 is the coefficient of friction at a reference fault slip velocity; a and b are frictional constitutive parameters, which respectively represent the effect of instantaneous and displacement-dependent changes in friction from V_0 to V ; θ is a state variable; and D_c is the critical slip distance. Frictional stability is determined in part by the parameter ($a-b$) for a finite step in velocity, expressed as (Dieterich, 1979; Marone, 1997; Ruina, 1983; Scholz, 1998)

$$a - b = \frac{\Delta\mu_{ss}}{\Delta \ln V} \quad (3)$$

The μ value defines the propensity for failure, while ($a-b$) values define the mode of slip, as stable, aseismically (i.e., $a-b > 0$), or unstable, seismically (i.e., $a-b < 0$; Kohli & Zoback, 2013; Samuelson & Spiers, 2012).

Abundant experimental studies have revealed the values of frictional strength and frictional stability of a variety of rock materials, such as shales, tuffs, carbonates, clays, mineral mixtures, and natural fault gouge. Behavior may be divided among three mineral groups: tectosilicates, carbonates, and phyllosilicates (Figure 1b; Boulton et al., 2012; Carpenter et al., 2015; Fang et al., 2016; Giorgetti et al., 2015; Ikari, et al., 2011, 2015; Kohli & Zoback, 2013; Moore & Lockner, 2011; Numelin et al., 2007; Samuelson & Spiers, 2012; Scuderi et al., 2013; Smith & Faulkner, 2010; Stesky et al., 1974; Tesei et al., 2014; Verberne et al., 2010;

Table 1
Relationships of Mineral Compositions, Frictional Stability, and Frictional Strength

Reference	Sample	σ_{eff} (MPa)	Mineral composition (wt.%)			V_{IP} ($\mu\text{m/s}$)	Ave. friction (μ_{SS})	Ave. stability ($a-b$)
			P-group	C-group	T-group			
(Fang et al., 2016)	Newberry Tuff_1	15	0.0%	0.0%	100.0%	1–30	0.616	0.0015
	Newberry Tuff_2	15	27.8%	14.4%	57.7%	1–30	0.612	0.0018
	Newberry Tuff_3	15	17.2%	3.5%	79.3%	1–30	0.623	0.0006
	Newberry Tuff_4	15	13.8%	0.5%	85.7%	1–30	0.643	0.0018
	Newberry Tuff_5	15	5.0%	0.4%	94.6%	1–30	0.660	0.0006
(Kohli & Zoback, 2013)	Barnett_1	10	7.1%	23.4%	69.5%	0.1–10	0.784	–0.0032
	Barnett_2	10	32.5%	22.7%	44.8%	0.1–10	0.511	0.0023
	Barnett_3	10	39.5%	0.3%	60.2%	0.1–10	0.465	0.0049
	Barnett_4	10	42.2%	0.0%	57.8%	0.1–10	0.432	0.0062
	Haynesville_1	10	26.1%	56.5%	17.4%	0.1–10	0.612	–0.0025
	Haynesville_2	10	48.7%	23.4%	27.9%	0.1–10	0.427	0.0076
	Haynesville_3	10	52.2%	26.6%	21.1%	0.1–10	0.402	0.0084
	Eagleford_1	10	13.0%	73.2%	13.8%	0.1–10	0.698	–0.0029
	Eagleford_2	10	28.7%	62.6%	8.7%	0.1–10	0.567	–0.0018
(Boulton et al., 2012; Figure 5)	CFR_GCS_U3P	31	31.7%	8.5%	59.8%	0.1–10	0.57	0.001
	CFR_GCS_U4F	31	58.6%	2.0%	39.4%	0.1–10	0.5	0.0036
	CFR_GCS_U4	30	20.8%	2.1%	77.1%	0.1–10	0.53	–0.0007
	CFR_GCT_U3	31	40.2%	5.9%	53.9%	0.1–10	0.31	0.0085
	CFR_WR_U3	31	19.4%	25.5%	55.1%	0.1–10	0.4	0.0063
	CFR_WR_U4	30	25.0%	7.0%	68.0%	0.1–10	0.555	–0.0008
(Tesei et al.; Viti et al., 2014)	I134	10	50.0%	50.0%	0.0%	1–300	0.52	0.0064
(Giorgetti et al., 2015; Figures 2 and 4a)	Talc_Cal1	5	0.0%	100.0%	0.0%	0.1–30	0.65	–0.0031
	Talc_Cal2	5	5.0%	95.0%	0.0%	0.1–30	0.56	0.0040
	Talc_Cal3	5	20.0%	80.0%	0.0%	0.1–30	0.51	0.0050
	Talc_Cal4	5	50.0%	50.0%	0.0%	0.1–30	0.25	0.0036
	Talc_Cal5	5	100.0%	0.0%	0.0%	0.1–30	0.20	0.0030
(Smith & Faulkner, 2010; Figures 6 and 10)	FG_L5.2	50	21.0%	44.0%	35.0%	0.1–1	0.42	0.0055
	FC_L4	25	5.0%	46.0%	49.0%	0.1–1	0.58	0.002
(Verberne et al., 2014; Figures 5 and 6)	XJ_limestone	50	3.0%	95.0%	2.0%	0.1–10	0.72	0.0028
	CaCO3_gouge	50	0.0%	98.0%	2.0%	0.1–10	0.73	0.0034
(Verberne et al., 2010; Tables 1 and 2)	SMG	30	29.0%	16.0%	55.0%	0.122–1.22	0.61	0.00445
	SSG	30	30.7%	2.0%	67.3%	0.122–1.22	0.59	0.00445
	NG	30	65.0%	0.0%	35.0%	0.122–1.22	0.42	0.00495
	SLG	30	2.0%	96.0%	2.0%	0.122–1.22	0.71	0.006
(Stesky et al., 1974; Ikari et al., 2011b; Table 3)	Westerly	49.9	5.0%	0.0%	95.0%	1–30	0.69	0.0021
	Berea SS	49.9	3.0%	4.0%	93.0%	1–30	0.93	–0.0003
	Indiana SS	49.9	2.0%	94.9%	3.0%	1–30	0.93	–0.0016
(Numelin et al., 2007)	A3	5	63.1%	2.3%	34.5%	10–50	0.65	0.0019
	A6	5	65.0%	8.9%	26.1%	10–50	0.42	0.0095
(Samuelson & Spiers, 2012)	NST_Soll1	35	47.0%	43.0%	10.0%	0.2–10	0.485	0.0026
	NST_Rot1	35	59.0%	0.0%	41.0%	0.2–10	0.540	0.0032
	NST_Rot2	35	24.0%	1.0%	75.0%	0.2–10	0.570	0.0028
	NST_Hard1	35	0.0%	8.0%	92.0%	0.2–10	0.670	0.0025
	NST_Sol/Hard	35	23.5%	25.5%	51.0%	0.2–10	0.620	0.0031
(Ikari et al., 2015)	Penn_Slate	50	54.0%	15.0%	31.0%	1–300	0.412	0.002
(Moore & Lockner, 2011, Figure 11a and Table A1)	Qrt_talc0	100	0.0%	0.0%	100.0%	0.01–1	0.710	–0.0002
	Qrt_talc5	100	5.0%	0.0%	95.0%	0.01–1	0.675	–0.0001
	Qrt_talc10	100	10.0%	0.0%	90.0%	0.01–1	0.660	0.0003
	Qrt_talc15	100	15.0%	0.0%	85.0%	0.01–1	0.615	–0.0010
	Qrt_talc25	100	25.0%	0.0%	75.0%	0.01–1	0.490	0.0016
	Qrt_talc50	100	50.0%	0.0%	50.0%	0.01–1	0.278	0.0066
	Qrt_talc75	100	75.0%	0.0%	25.0%	0.01–1	0.150	0.0050
	Qrt_talc100	100	100.0%	0.0%	0.0%	0.01–1	0.130	0.0034
(Scuderi et al., 2013)	Dol_Cor	10	0.0%	100.0%	0.0%	3–300	0.659	0.0025

Note. (1) Mineral composition data are taken within three effective digit numbers. (2) T, C, and P are normalized using the equation: $T/(T + C + P) * 100\%$. (3) Steady state friction and frictional stability ($a-b$) are averaged over multiple velocity steps. (4) Values might not add 100% due to rounding and reporting of trace phases, amorphous mineraloid, neso-cyclo-soro-ino-silicate. (5) Values are normalized to fit the ternary diagram.

Verberne et al., 2014; Viti et al., 2014). These frictional strength and stability values follow a reversal relationship (Figure 1a). The time or rate dependence of frictional strength is due to processes that affect the true area of solid-solid contact between the sliding surfaces. Microphysical models explain these experimental observations by examining the mechanics of surface contact and rheology of microstructure of crystalline phases during shear deformation. This suggests that the frictional stability of a simulated fault gouge is associated with shear-induced dilation or compaction (Niemeijer & Collettini, 2013; Niemeijer & Spiers, 2007). This volume change of fracture aperture may suggest a hydraulic conductivity change. Hence, the frictional strength and stability values may be linked to permeability evolution of a fracture during shearing.

Previous experiments have explored friction-permeability relationships of carbonate-rich and phyllosilicate-rich shales during shear slip, suggesting that carbonate-rich shale has a higher frictional strength, but lower frictional stability and smaller permeability reduction than that of phyllosilicate-rich shale (Fang et al., 2017). The numerical study also indicates that quartz-rich gouge has high tendency toward dilation while talc dilates with increased slip rate but followed by a rapid compaction (Wang et al., 2017). These results imply the influence of mineralogy on friction-stability-permeability relationships. However, it is still unclear how the role of each mineral group (i.e., tectosilicate, carbonate, and phyllosilicate content) plays in this relationship and still uncertain whether or not a systematic relationship of friction-stability-permeability relationships of fractures can be constrained.

In this study, we explore friction-stability-permeability relationships with respect to mineralogical compositions of fractures through a series of direct-shear experiments on natural rocks with saw-cut fracture surfaces. These rocks are composed of distinct mineralogical compositions, as do sintered fractures with specially controlled weight percentages of mineral groups. In particular, we address questions including the following: Can mineralogical compositions suggest the frictional strength, stability, and shear permeability evolution of fractures? What is the implication of the friction-stability-permeability relationship to fluid rock interaction in fluid-injection-involved engineering activities, such as long-term heat recovery and geological sequestration of CO₂?

2. Experimental Method

In the following we define experimental assumptions, introduce sample materials and methods of preparation, and finally define the experimental setup and procedures.

2.1. Assumptions

The experimental conditions and data analysis are based on the following assumptions: (1) Frictional strength and stability are primarily controlled by three mineralogical end-members: carbonates (*C*), tectosilicates (*T*), and phyllosilicates (*P*) while keeping other factors (e.g., effective normal stress, fracture roughness, and temperature) constant (Figure 1). (2) The sintered fractures comprise an assemblage of three mineral groups: carbonates, tectosilicates, and phyllosilicates. The percentage of each mineral group is defined from lithoface classifications of shale rock in Figure 2 (Gamero-Diaz et al., 2013). (3) The frictional strength of sintered samples is shown to be representative of natural samples with the same lithology. The frictional strength of natural Green River shale and sintered Green River shale (powdered and reconsolidated) shows a difference of <10%, suggesting a reliable analogue (Figure 3). (4) The linkage between the evolution of frictional strength, stability, and permeability is explored in the brittle regime where mechanical controls dominate response and thermally and chemically activated effects are too slow to be manifest.

2.2. Sample Materials and Preparation

In this experiment, we prepare two types of samples: (1) intact natural samples and (2) sintered samples. We collect six intact natural samples including five shales (i.e., Green River shale, Opalinus claystone, Marcellus shale, Tournemire shale, and Longmaxi shale) and one tuff (i.e., Newberry tuff). The Green River shale is deposited in a freshwater lacustrine environment and is recovered from the sequence at Grand Junction, Colorado. The Opalinus shale, known as a clay-rich caprock, is taken from horizontal borehole (BEZ-G50) at the Mont Terri underground rock laboratory in Switzerland. The Marcellus shale is taken from outcrop from the Middle Devonian Marcellus Formation at Frankstown, PA (New Enterprise Quarry off Locke Mountain Road, Coordinates: N40°26'00", W78°20'28"). The Tournemire shale sample is cored from a fault zone in the shale formations at Tournemire Underground Research Laboratory in France. The Longmaxi shale sample

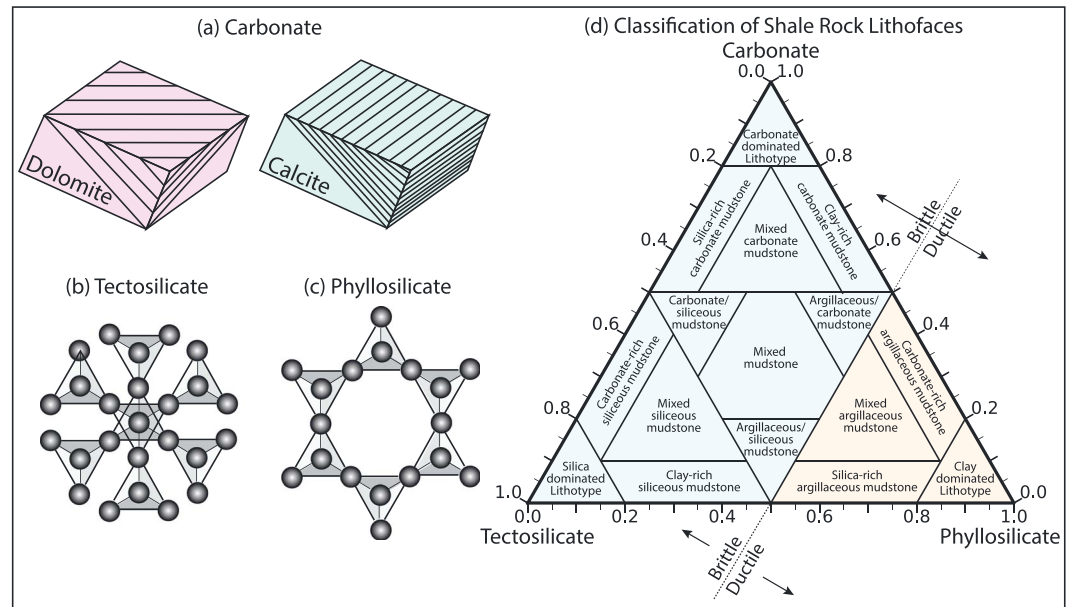


Figure 2. (a) Crystal structure of dolomite. Dolomite has almost exactly the same structure as calcite except that layers of magnesium and calcium atoms alternate. The alternation means a complete unit cell of dolomite is not the same as a cleavage rhombohedron. (b) The tectosilicates or framework silicates have a structure wherein all of the four oxygens of SiO₄⁻⁴ tetrahedra are shared with other tetrahedra. (c) The basic structure of the phyllosilicates is based on interconnected six member rings of SiO₄⁻⁴ tetrahedra that extend outward in infinite sheets. (d) Ternary diagram of lithofaces classification with the three apexes representing the components carbonate, tectosilicate, and phyllosilicate (modified from Gamero-Diaz et al., 2013).

is collected from the major gas production formation, Sichuan Province, China. The Newberry tuff is cored from well N2 at Newberry geothermal site, Oregon.

The sintered samples are consolidated from five different minerals: dolomite, calcite, albite, quartz, and illite that are common in major fault zones. The mineral chips are purchased from Ward Science Company (Figure 4a) and then powdered with a particle size less than 100 μm. Based on the weight percentage in

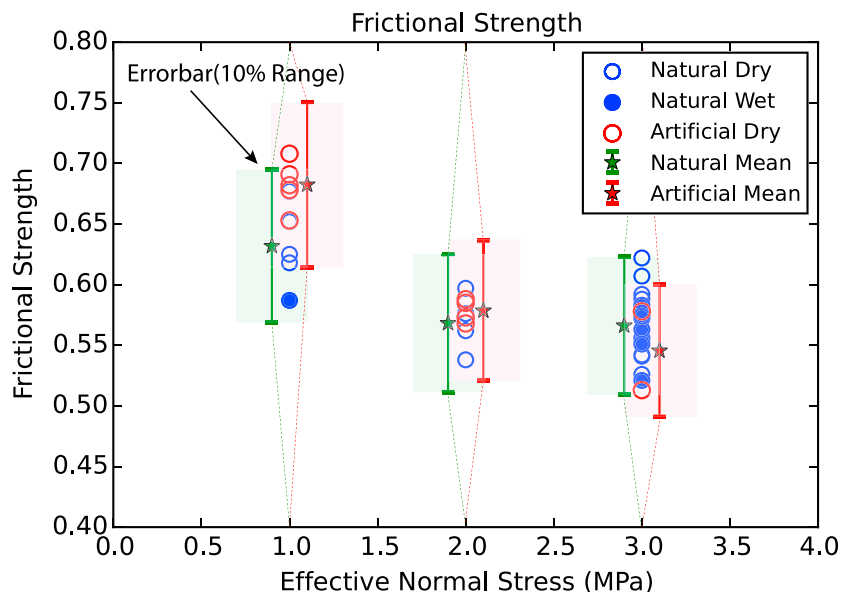


Figure 3. Frictional strength of both artificially consolidated and natural Green River shale rocks under different effective normal stress. The error bar bounds 10% of the average frictional strength.

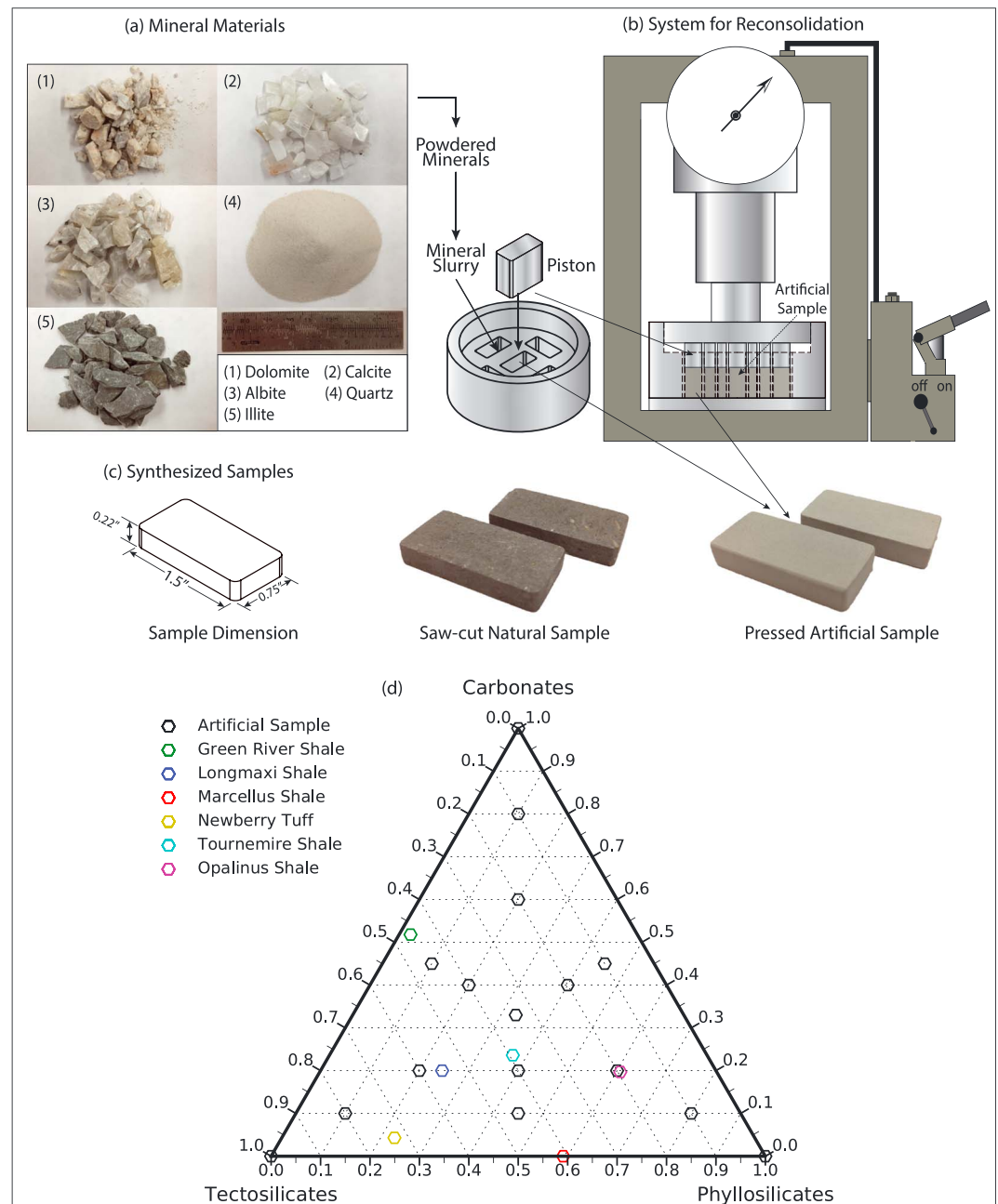


Figure 4. (a) Minerals for artificial samples. (b) System for reconsolidation comprising a pressuring system, sample vessel, draining base, and piston. (c) Dimension of saw-cut natural and artificial samples. (d) Ternary diagram of mineral groups (tectosilicate, carbonate, and phyllosilicate) for both natural samples and artificial samples (wt.% data is listed in Table 4). (e) Experimental setup to measure friction-permeability evolution: Pump A controls the normal stress applied on the fracture. Pump B provides the source of shear stress applied on the fracture. Pump C injects the fluid at a prescribed flow rate or pressure, allowing the fluid source located at the origin of the fracture and flow along the fractures.

Figure 2, the powders of each mineral phase are uniformly mixed with deionized water. The mixed mineral slurry is filled into the pressing vessel, and then drained and consolidated under an overburden stress of 150 MPa (Figure 4b). When consolidation ceases, the samples are removed from the pressure vessel and dried at room temperature for 48 hr. The natural samples are saw cut into twin coupons with a dimension of 0.22 inch × 1.5 inch × 0.75 inch (0.5588 cm × 3.81 cm × 1.905 cm; Figure 4c). The artificial samples are directly pressed into the same dimension as that of natural samples. The planar surfaces of the coupons

Table 2
Mineral Compositions (wt.%) of Natural Samples

Samples minerals	Green shale	River shale	Opalinus shale	Marcellus shale	Tournemire shale	Longmaxi shale	Newberry tuff
Quartz	14.9		16.5	36.1	31.3	50.9	30.0
Analcime	16.7		0.0	0.0	0.0	0.0	0.0
Anorthite	7.8		0.0	0.0	0.0	0.0	0.0
Albite	0.0		0.0	0.0	0.0	3.7	42.4
Orthoclase	0.0		2.4	0.0	6.4	0.0	0
Microcline	6.5		0.0	0.0	0.0	0.0	0
Dolomite	39.4		0.0	0.0	0.0	3.4	2.8
Calcite	12.4		19.7	0.0	23.6	16.7	1.6
Muscovite	0.0		42.4	10.4	3.1	0.0	0
Illite	2.3		3.6	44.8	23.3	24.6	0
Chlorite	0.0		0.0	0.0	3.7	0.0	22.2
Clinochlore	0.0		3.9	0.0	0.0	0.0	0.6
Kaolinite	0.0		10.9	3.9	7.0	0.0	0
Montmorillonite	0.0		0.0	0.0	0.0	0.0	0
Others	0.0		0.6	4.8	1.8	0.7	0.3

are uniformly roughened with grinding powder (#60 Grit) to ensure the surface roughness of the same order. The mineral compositions of the natural samples are characterized via X-ray diffraction, and the data are listed in Table 2. The basic properties of those samples are listed in Table 3. The weight percentage of each group of all samples is illustrated in Figure 4d.

2.3. Experimental Setup and Procedure

The friction-permeability experiments are conducted in a triaxial testing apparatus that independently applies normal stress and differential (end-to-end) pore pressure, while the sample is sheared at a prescribed velocity (Figure 5). This allows the concurrent measurement of the evolution of fracture permeability and friction. The sample coupons are packed within a pair of steel shearing platens. The initial offset of platens is ~8 mm for slip displacement during sliding. The platen-offset gap is filled with filler as a seal. The side and bottom contacts between the sample coupon and the platen surfaces are packed with Teflon to prevent fluid leakage. The assembled platens are packed within a membrane to isolate from the confining fluid. A steel sleeve covers the load cell to prevent the effect of applied confining pressure.

To be consistent with the applied stress conditions of previous experimental studies (Fang et al., 2017), we apply a confining stress (normal stress) of 3 MPa and set a constant upstream fluid pressure during axial shear displacement (at constant rate). The minimum flow rate of each pump (ISCO 500D) is 0.001 ml/min, and the display resolution of the pump pressure transducer is 1.0 kPa. A load cell with a resolution of 0.3 kPa is used to measure the axial stress. At room temperature, the minimum measurable permeability is $1.0 \times 10^{-16} \text{ m}^2$.

We conduct velocity-stepping experiments to compare the hydraulic behavior response to varying velocities for both natural and sintered samples. The shear velocity is set to 10 $\mu\text{m/s}$ (monotonic) and switched between down-steps and up-steps between 1 and 10 $\mu\text{m/s}$, until a displacement of ~6 to 7 mm is reached. All experiments are performed at room temperature (25 °C), with shear displacements recorded by linear variable differential transformer located outside the vessel.

Table 3
Basic Mechanical and Hydraulic Properties of Natural Samples

Properties samples	Young's modulus (GPa)	Porosity ϕ (%)	Matrix perm (k_{matrix} , m^2)	Reference
GRS	24	3.5%	$1.0\text{--}5.0 \times 10^{-19}$	(Yildirim, 2014)
NRT	31	2–4%	4.0×10^{-19}	(Wang et al., 2016)
LMX	25	3.9%	1.0×10^{-20}	(Jia et al., 2018)
TNM	7.7	8–12%	1.0×10^{-20}	(Guglielmi, Elsworth, et al., 2015)
MCS	25	6.25%	$1.0\text{--}5.0 \times 10^{-19}$	(Yildirim, 2014)
OPS	10–12	2–5%	4.5×10^{-21}	(Keller, 2016)

Table 4
Mineral Compositions (wt.%) of Artificial Samples

Sample number	Tectosilicate (wt. %)			Carbonate (wt. %)			Phyllosilicate (wt. %)	
	Quartz	Albite	Total	Calcite	Dolomite	Total	Illite	Total
AS001	40.0	40.0	80.0	5.0	5.0	10.0	10.0	10.0
AS002	5.0	5.0	10.0	5.0	5.0	10.0	80.0	80.0
AS003	5.0	5.0	10.0	40.0	40.0	80.0	10.0	10.0
AS004	16.65	16.65	33.3	16.65	16.65	33.3	33.3	33.3
AS005	10.0	10.0	20.0	30.0	30.0	60.0	20.0	20.0
AS006	10.0	10.0	20.0	10.0	10.0	20.0	60.0	60.0
AS007	30.0	30.0	60.0	10.0	10.0	20.0	20.0	20.0
AS008	5.0	5.0	10	22.5	22.5	45.0	45.0	45.0
AS009	22.5	22.5	45.0	22.5	22.5	45.0	10.0	10.0
AS0010	22.5	22.5	45.0	5.0	5.0	10.0	45.0	45.0
AS0011	10.0	10.0	20.0	20.0	20.0	40.0	40.0	40.0
AS0012	20.0	20.0	40.0	20.0	20.0	40.0	20.0	20.0
AS0013	20.0	20.0	40.0	10.0	10.0	20.0	40.0	40.0
AS0014	0.0	0.0	0.0	50.0	50.0	100.0	0.0	0.0
AS0015	0.0	0.0	0.0	0.0	0.0	0.0	100.0	100.0

3. Results and Discussions

In the following, we first interpret measurements of concurrent flow and deformation to recover friction-stability-permeability evolution in the context of rate-state friction models. We then correlate these friction-stability-permeability relationships with mineral assemblage to explore how mineralogy may control permeability evolution and link this with seismicity.

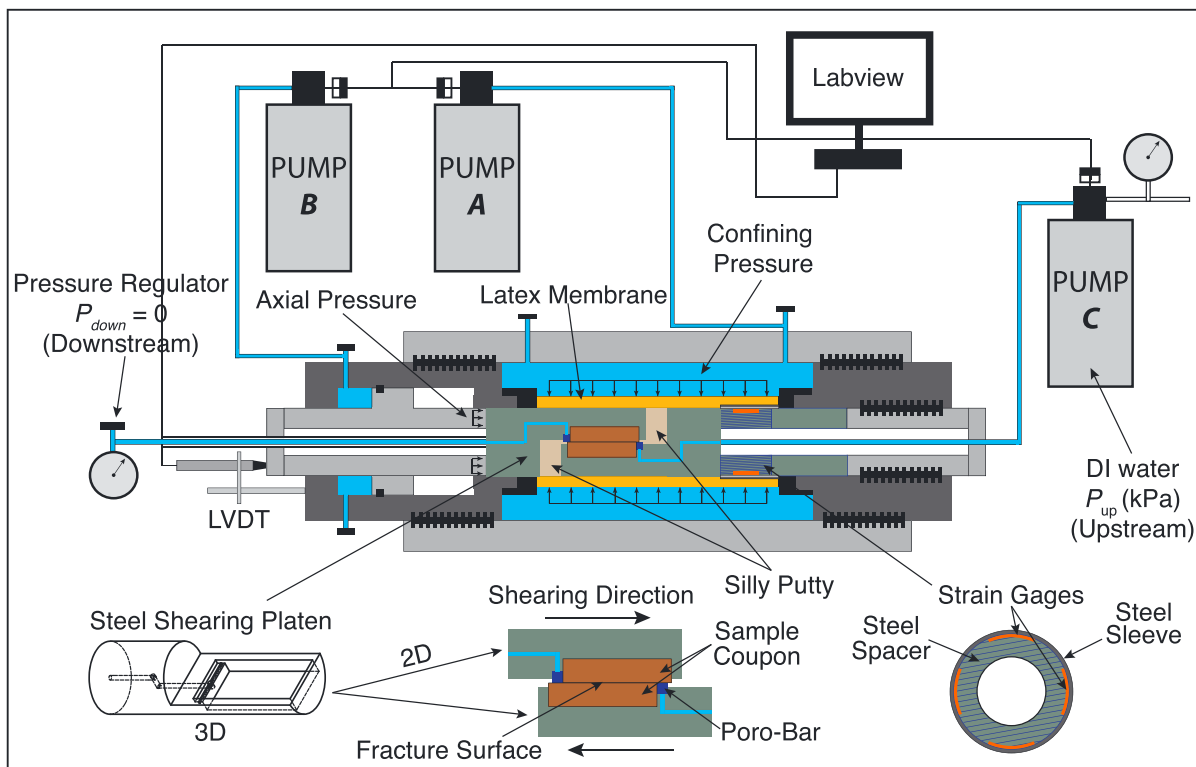


Figure 5. Experimental apparatus to measure friction-permeability evolution: Pump A controls the normal stress applied to the fracture. Pump B provides the source of shear stress applied on the fracture. Pump C injects the fluid at a prescribed flow rate or pressure into the upstream extent of the fracture.

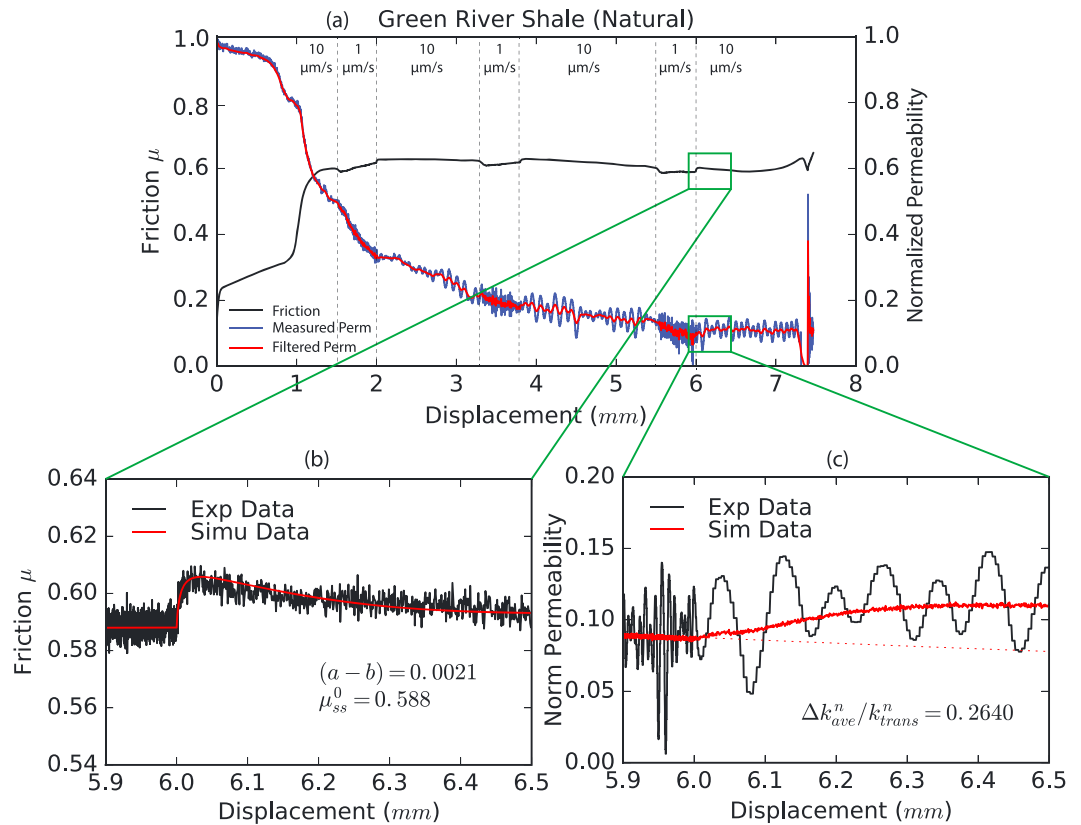


Figure 6. (a) Net friction and permeability evolution during slip (the black curve indicates measured friction, the blue curve indicates measured permeability, and the red curve indicates filtered data of measured permeability). (b) Frictional response to velocity change from 1 to 10 $\mu\text{m/s}$. (c) Permeability change with respect to velocity change from 1 to 10 $\mu\text{m/s}$.

3.1. Analysis and Discussion

Frictional strength and stability are evaluated from equations (1) to (3). The measured fracture permeability k_m (m^2) is expressed in terms of averaged hydraulic aperture b_m (m) based on the cubic law of a single fracture:

$$b_m = - \left(\frac{12\mu_{vis} \cdot L(t) \cdot Q(t)}{W \cdot \Delta P_f} \right)^{1/3} \quad (4)$$

Table 5
Results of Frictional Stability and Transient Permeability Changes for Natural Rock Samples

Sample	Normal stress (MPa)	Loading velocity ($\mu\text{m/s}$)	Steady state friction (μ_{ss})	Frictional stability ($a - b$)	k_0 (10^{-12}m^2)	Δk_n (-)
GRS	3.0	1.0 to 10.0	0.606	0.001	69.503	0.01839
GRS	3.0	1.0 to 10.0	0.614	0.0005	69.503	0.01741
GRS	3.0	1.0 to 10.0	0.588	0.0021	69.503	0.02302
NBR	3.0	1.0 to 10.0	0.73	0.002	90.867	0.02497
NBR	3.0	1.0 to 10.0	0.752	0.0012	90.867	0.03316
LMX	3.0	1.0 to 10.0	0.61	0.0034	77.541	0.03200
LMX	3.0	1.0 to 10.0	0.545	0.0056	77.541	0.02830
TNM	3.0	1.0 to 10.0	0.432	0.009	14.814	0.02985
TNM	3.0	1.0 to 10.0	0.47	0.011	14.814	-0.14445
MCS	3.0	1.0 to 10.0	0.505	0.007	61.416	0.00019
MCS	3.0	1.0 to 10.0	0.52	0.0075	61.416	-0.00432
OPS	3.0	1.0 to 10.0	0.521	0.0152	8.801	0.00067
OPS	3.0	1.0 to 10.0	0.442	0.013	8.801	-0.00160

Table 6
Data of Frictional Stability and Transient Permeability Changes for Artificial Rock Samples

Sample	Normal stress (MPa)	Loading velocity ($\mu\text{m/s}$)	Steady state friction (μ_{ss})	Frictional stability ($a-b$)	k_0 (10^{-12} m^2)	Δk_n (-)
AS001	3.0	1.0 to 10.0	0.815	0.004	0.187	0.03009
AS002	3.0	1.0 to 10.0	0.475	0.016	0.376	0.01199
AS003	3.0	1.0 to 10.0	0.7	0.015	3.558	0.00628
AS004	3.0	1.0 to 10.0	0.574	0.0083	0.914	0.00978
AS005	3.0	1.0 to 10.0	0.564	0.0151	1.989	-0.00820
AS006	3.0	1.0 to 10.0	0.511	0.0111	0.449	0.02414
AS007	3.0	1.0 to 10.0	0.586	0.006	1.568	0.00512
AS008	3.0	1.0 to 10.0	0.715	0.015	0.492	0.03442
AS009	3.0	1.0 to 10.0	0.765	0.009	2.87	0.00673
AS010	3.0	1.0 to 10.0	0.75	0.022	6.609	-0.00144
AS011	3.0	1.0 to 10.0	0.782	0.0211	0.655	-0.01650
AS012	3.0	1.0 to 10.0	0.634	0.0084	1.82	0.00655
AS013	3.0	1.0 to 10.0	0.648	0.0098	3.064	0.01618
AS014	3.0	1.0 to 10.0	0.768	0.0063	19.585	0.00351
AS015	3.0	1.0 to 10.0	0.416	0.0143	3.54	0.00255

$$k_m = \frac{b_m^2}{12} \quad (5)$$

where μ_{vis} (Pa·s) is the viscosity of fluid, $L(t)$ (m) is the contact length of the fracture surface, W (m) is the fracture width, $Q(t)$ (m^3/s) is the measured flow rate, and ΔP_f (Pa) is the differential pressure between the upstream and downstream extent of the fracture.

By solving equations (1) to (3), we model a (shearing) velocity step of each shale sample to confirm the frictional parameters. Meanwhile, we define two terms representing permeability change as follows,

$$\Delta k_n^i = \frac{k_{real}^i - k_{sim}^i}{k_0} \quad (6)$$

where Δk_n^i refers to the permeability change normalized to the initial fracture permeability k_0 before shearing, k_{real}^i is the measured permeability after the velocity step, and k_{sim}^i is the simulated permeability that is assumed for unchanged velocity (i.e., no velocity step). Index i refers to the i th velocity step. The data fitted-based k_{sim}^i is estimated from the evolving aperture b_{evo} during shear slip, considering velocity-dependent compaction or dilation (Fang et al., 2017). As frictional parameters evolve with shearing, to correlate the transient permeability change to the concurrent frictional parameters, it is necessary to calculate the relative permeability change with respect to the permeability value at the point immediately before the shear velocity step:

$$\frac{\Delta k^i}{k_0^i} = \frac{k_{real}^i - k_{sim}^i}{k_0^i} \quad (7)$$

where Δk^i is the absolute permeability change from before until after the velocity step and k_0^i is a reference permeability before the velocity step is applied. Figure 6a shows the results of one sample as an example of the net friction and permeability evolution with displacement. The calculated net fracture permeability monotonically decreases with displacement, consistent with previous observations (Fang et al., 2017). Local frictional change and permeability evolution in response to shear velocity change are shown in Figures 6b and 6c. The permeability change in each velocity step is normalized against the reference permeability in the state immediately before the velocity-step induced change. The measured and modeled frictional parameters and permeability change of each sample are listed in Tables 5 and 6.

The analyzed frictional parameters and transient permeability change in response to velocity change are shown in Figure 7 with respect to the selected mineral groups: phyllosilicates, carbonates, and tectosilicates. Frictional strength μ and transient permeability change Δk_n and $\Delta k_n/\Delta k_0^i$ decrease with phyllosilicate content but increase with tectosilicate content. In contrast, a reverse trend is observed for frictional stability ($a-b$). However, the role of carbonate is distinct from the other two mineral groups. The trend between

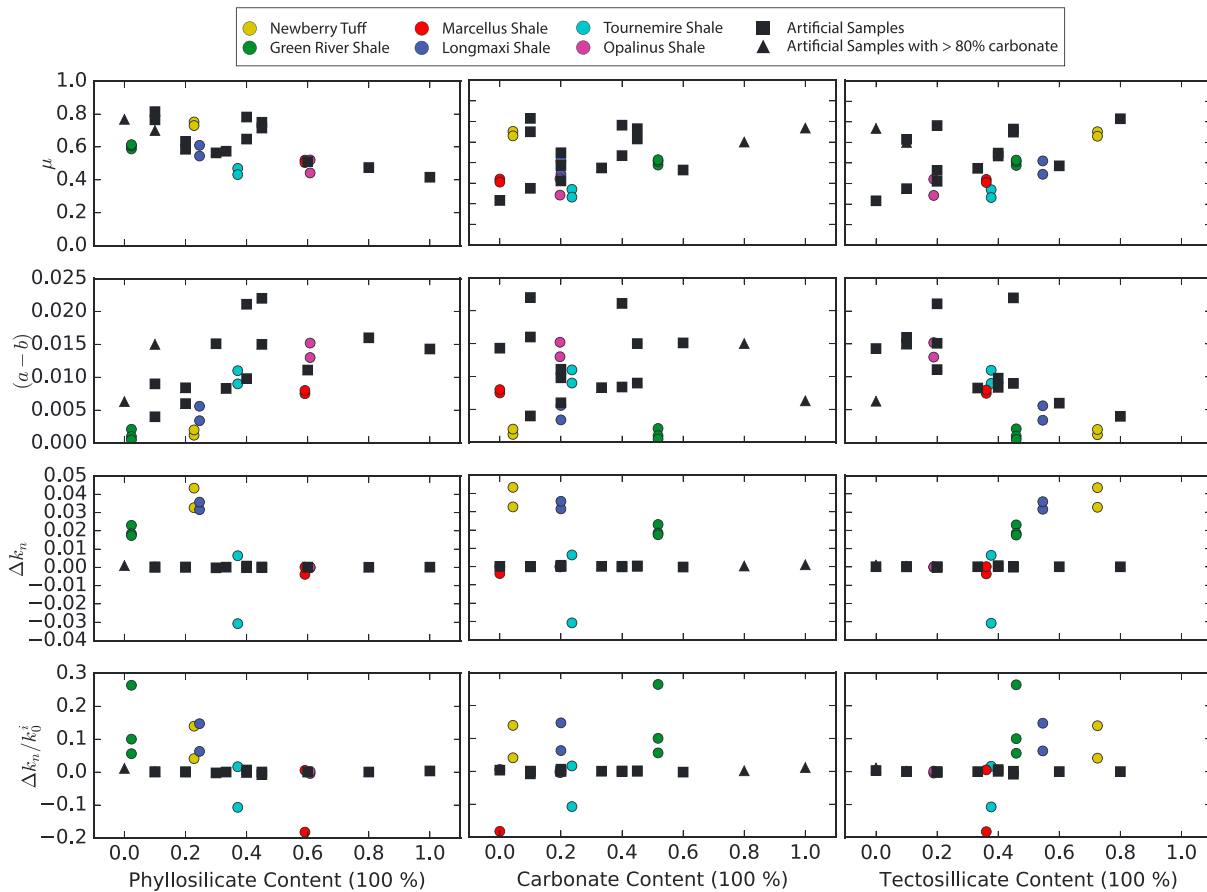


Figure 7. Effect of mineral composition on friction response (i.e., μ and $(a-b)$) and transient permeability evolution (i.e., Δk_n and $\Delta k_n/\Delta k_0^i$) in response to shear velocity change. (a) Effect of phyllosilicate content. (b) Effect of carbonate content. (c) Effect of tectosilicate content.

carbonate content and permeability change is not clear. The permeability changes decrease with both frictional strength and stability, implying that in the very shallow crust (i.e., low normal stress and low temperature), slip reactivation in calcite-bearing fault gouges is difficult and is unlikely to induce seismic events—and permeability is reduced during the resulting aseismic slip.

As surface contact state, which determines the flow path, is reflected in the frictional strength and stability, we directly correlate the permeability change with friction in Figure 8. The permeability change Δk has a positive correlation with concurrently measured frictional strength μ but a negative correlation with the corresponding frictional stability $(a-b)$. This intrinsic linkage of friction and permeability change is directly determined by the asperity contact state and the material properties (e.g., mechanical and swelling) that control the mechanical behaviors of fracture asperities. However, it is worth noting that the magnitude of permeability change in the natural samples is much larger than that of the artificial samples (shown as the solid black symbols in Figures 7 and 8)—this is due to the difference in the surface textures as schematically illustrated in Figure 9.

In summary, with known mineralogical compositions comprising the fracture, the frictional strength and stability of fractures can be estimated. Shear failure is less likely to occur for fractures with higher content of tectosilicates. However, once failure initiates, the fracture is more likely slip unstably. This process is opposite that for fractures with higher clay content—where the fracture is easier to reactivate and will slip stably. When an unstable fracture slides at an accelerating rate, the transient change in fracture permeability can be speculated—those richer in tectosilicates exhibit larger permeability enhancement.

3.2. Implication

Friction-permeability relationships defined with respect to mineralogy imply that fluid-rock interactions in fault zones may systematically impact the likelihood of reactivation, the mode of deformation as seismic or

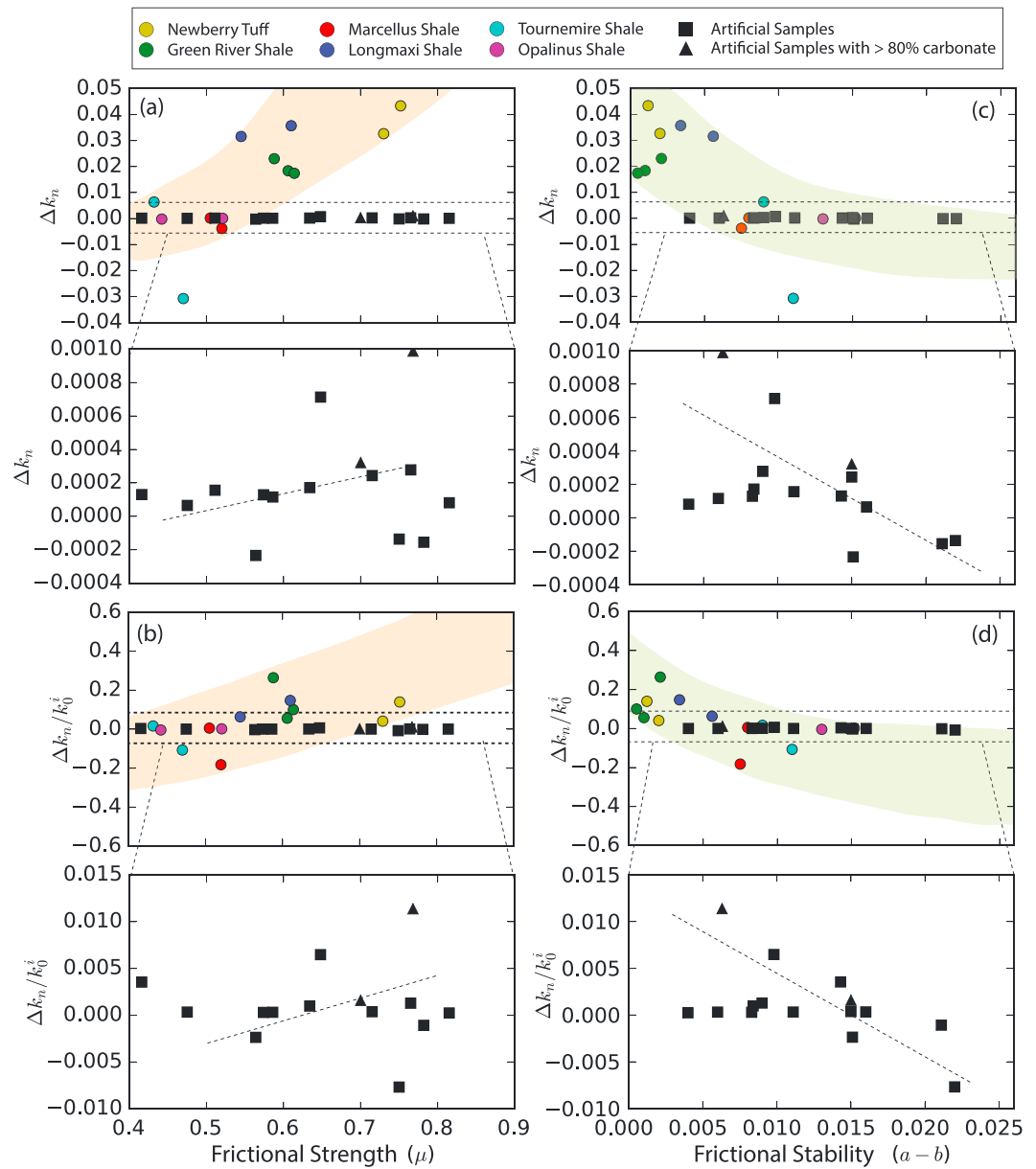


Figure 8. (a and b) Correlation between frictional strength (μ) and permeability evolution (Δk_n and $\Delta k^i/\Delta k_0^i$). (c and d) Correlation between frictional stability ($a-b$) and permeability evolution (Δk_n and $\Delta k^i/\Delta k_0^i$).

aseismic, and the corresponding sense of permeability evolution. During the evolution of a natural fault, fluids can react with fault rocks. For example, fine-grained cataclasites in the fault core (Evans & Chester, 1995) may transform to new mineral phases (e.g., phyllosilicate-rich) and structures (e.g., foliation) that weaken the fault (Collettini et al., 2008) and impact its mode of deformation. The impact of such fluid-rock interaction is represented in the substitution of mineralogical compositions selected in this work. For instance, when phyllosilicate-rich materials result from aluminosilicates, frictional strength is reduced due to the change in mineralogical content. Moreover, precipitation of new minerals (e.g., carbonates) decreases the fracture aperture and potentially its permeability. Dissolution, however, can increase porosity and permeability (Nogues et al., 2013) and potentially weaken the fault by reducing the fault frictional strength if sufficient dissolution occurs on the interlocked and cemented carbonate (i.e., the carbonate content is reduced). Natural fluid-rock interaction process in fault zones operate over geologic time scales (Kerrich, 1986; Lin et al., 2003). However, anthropogenic fluid-injection (i.e., enhanced

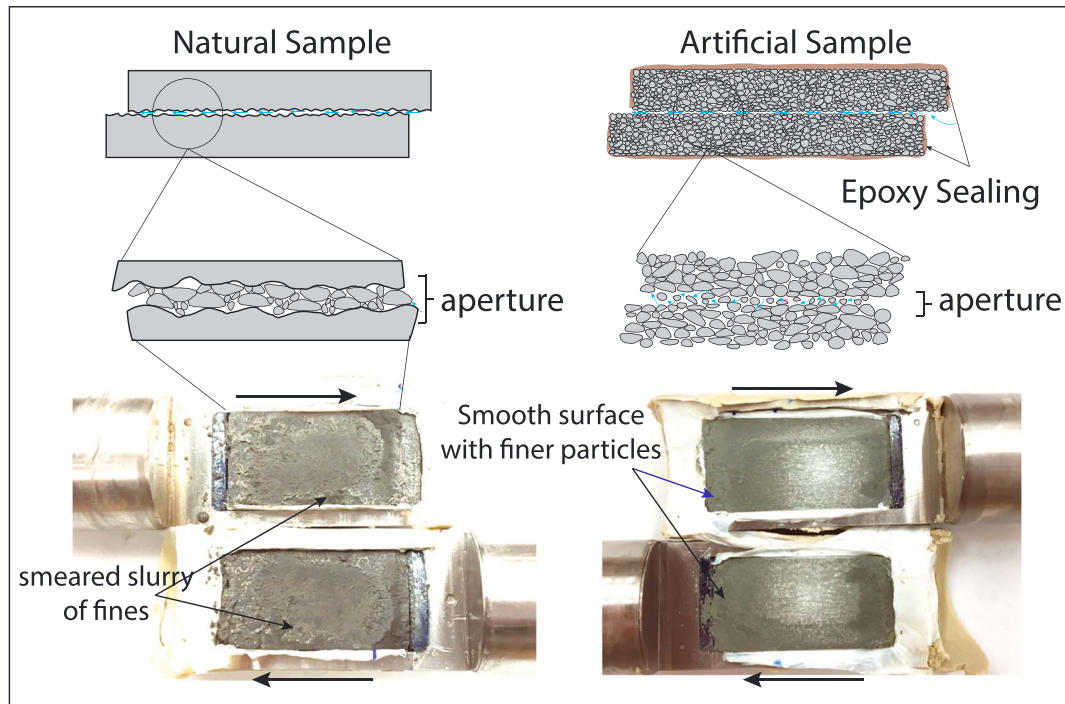


Figure 9. Schematic illustration of fracture surface texture of natural samples and artificial samples.

geothermal energy recovery and geological sequestration of CO₂) may accelerate these transformations with fluids pushed far from equilibrium. In such cases, we expect (1) friction evolution due to silica dissolution on fault surfaces where interactions exist between the injected water and the reservoir rock over a long-term fluid circulation (Xu et al., 2009) and (2) a significant change in frictional strength of faults may result from major carbonate precipitation in the fault damage zone due to rapid CO₂ leakage and degassing in a CO₂ storage system (Bakker et al., 2016).

Thus, a new closed mechanical-hydro-chemical coupling is speculated via linking the friction, mineralogy, and permeability of fault surfaces (Figure 10): (1) pore pressure grows in a fault zone, initiating fault slip at a critical state (Mohr-Coulomb criterion); (2) fault frictional behaviors, controlled by fault minerals (Ikari et al., 2011), define the mode of shear slip and its simultaneous permeability change; (3) altered fault permeability leads to a changed flow rate, breaking the equilibrium of initial mineral dissolution or precipitation (Ellis et al., 2013); and (4) newly formed mineral phases on fracture surfaces, in return, adjusts the frictional behaviors.

4. Conclusion

We report a series of direct-shear experiments with concurrent measurement of permeability to probe mineralogical controls on frictional strength, stability, and permeability. These are conducted on saw-cut fractures in natural rocks with distinct mineral compositions as well as sintered samples with predefined mineralogical mixtures. Friction-permeability relationships are strongly controlled by mineralogy. Given the experimental conditions of low effective normal stress, room temperature, and saw-cut planar fracture geometry, frictional strength and permeability change upon reactivation decrease with phyllosilicate content but increase with tectosilicate content. In contrast, the reverse trend is observed for frictional stability (*a-b*). However, the effect of carbonate content on frictional stability and transient permeability change is different. The permeability change decreases with carbonate content while both frictional strength

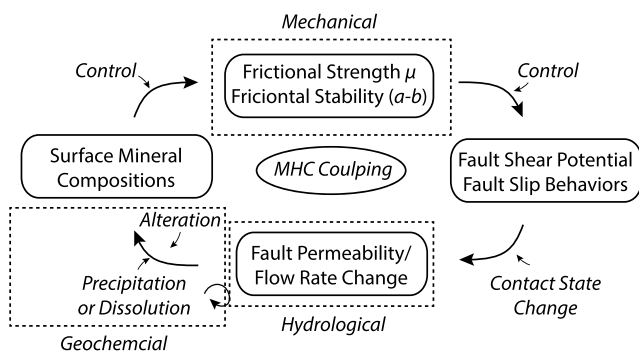


Figure 10. Schematic diagram of new mechanical-hydrological-chemical (MHC) coupling logic.

and stability increase. The permeability change always decreases with an increase in frictional stability. With this relationship, we speculate that planar fractures with low frictional stability exhibit permeability enhancement after seismic slip in the frame of rate-state friction theory. This relationship implies a new mechanical-hydro-chemical coupling loop via a linkage of frictional properties, mineralogy, and permeability. However, it is worth noting that friction-permeability relationships are complex and may also be affected by other external factors such as fracture surface roughness and material mechanical properties, which demands further experimental efforts.

Acknowledgments

We thank Chris Marone for help, insightful discussions, and suggestions on the conduct of experiments. We thank Steve Swavely for help in the laboratory. We thank the Editor Andre Revil for handling the manuscript and two anonymous reviewers whose careful reading and constructive comments helped improved the work. This work is a partial result of support provided by DOE grant DE-FE0023354. This support is gratefully acknowledged. The data for this paper are presented in the table.

References

- Bakker, E., Hangx, S. J. T., Niemeijer, A. R., & Spiers, C. J. (2016). Frictional behaviour and transport properties of simulated fault gouges derived from a natural CO₂ reservoir. *International Journal of Greenhouse Gas Control*, *54*, 70–83. <https://doi.org/10.1016/j.ijggc.2016.08.029>
- Barton, N., Bandis, S., & Bakhtar, K. (1985). Strength, deformation and conductivity coupling of rock joints. *International Journal of Rock Mechanics and Mining Sciences*, *22*(3), 121–140. [https://doi.org/10.1016/0148-9062\(85\)93227-9](https://doi.org/10.1016/0148-9062(85)93227-9)
- Ben-David, O., Cohen, G., & Fineberg, J. (2010). The dynamics of the onset of frictional slip. *Science*, *330*(6001), 211–214. <https://doi.org/10.1126/science.1194777>
- Boulton, C., Carpenter, B. M., Toy, V., & Marone, C. (2012). Physical properties of surface outcrop cataclastic fault rocks, Alpine Fault, New Zealand. *Geochemistry, Geophysics, Geosystems*, *13*, Q01018. <https://doi.org/10.1029/2011GC003872>
- Brune, J. N. (1970). Tectonic stress and the spectra of seismic shear waves from earthquakes. *Journal of Geophysical Research*, *75*(26), 4997–5009. <https://doi.org/10.1029/JB075i026p04997>
- Carpenter, B. M., Saffer, D. M., & Marone, C. (2015). Frictional properties of the active San Andreas Fault at SAFOD: Implications for fault strength and slip behavior. *Journal of Geophysical Research: Solid Earth*, *120*, 1–17. <https://doi.org/10.1002/2015JB011963>
- Collettini, C., Cardellini, C., Chiodini, G., De Paola, N., Holdsworth, R. E., & Smith, S. A. F. (2008). Fault weakening due to CO₂ degassing in the Northern Apennines: Short- and long-term processes. *Geological Society of London, Special Publication*, *299*(1), 175–194. <https://doi.org/10.1144/SP299.11>
- Cornet, F. H., Helm, J., Poitrenaud, H., & Etchecopar, A. (1997). Seismic and aseismic slips induced by large-scale fluid injections. *Pure and Applied Geophysics*, *150*(3–4), 563–583. <https://doi.org/10.1007/s000240050093>
- Davis, E. E., Becker, K., Wang, K., & Carson, B. (1995). Long-term observations of pressure and temperature in Hole 892B, Cascadia accretionary prism. In *Proceedings of the Ocean Drilling Program. Scientific results* (Vol. 146, pp. 299–311). College Station, TX: Ocean Drilling Program.
- Dieterich, J. H. (1978). Time-dependent friction and the mechanics of stick-slip. *Pure and Applied Geophysics PAGEOPH*, *116*(4–5), 790–806. <https://doi.org/10.1007/BF00876539>
- Dieterich, J. H. (1979). Modeling of rock friction: 1. Experimental results and constitutive equations. *Journal of Geophysical Research*, *116*(4–5), 790–806. <https://doi.org/10.1007/BF00876539>
- Ellis, B. R., Fitts, J. P., Bromhal, G. S., McIntyre, D. L., Tappero, R., & Peters, C. A. (2013). Dissolution-driven permeability reduction of a fractured carbonate Caprock. *Environmental Engineering Science*, *30*(4), 187–193. <https://doi.org/10.1089/ees.2012.0337>
- Evans, J. P., & Chester, F. M. (1995). Fluid-rock interaction in faults of the San Andreas system: Inferences from San Gabriel fault rock geochemistry and microstructures. *Journal of Geophysical Research*, *100*(B7), 13,007–13,020. <https://doi.org/10.1029/94JB02625>
- Fang, Y., den Hartog, S. A. M., Elsworth, D., Marone, C., & Cladouhos, T. (2016). Anomalous distribution of microearthquakes in the Newberry Geothermal Reservoir: Mechanisms and implications. *Geothermics*, *63*, 62–73. <https://doi.org/10.1016/j.geothermics.2015.04.005>
- Fang, Y., Elsworth, D., Wang, C., Ishibashi, T., & Fitts, J. P. (2017). Frictional stability-permeability relationships for fractures in shales. *Journal of Geophysical Research: Solid Earth*, *122*, 1760–1776. <https://doi.org/10.1002/2016JB013435>
- Faoro, I., Niemeijer, A., Marone, C., & Elsworth, D. (2009). Influence of shear and deviatoric stress on the evolution of permeability in fractured rock. *Journal of Geophysical Research*, *114*, B01201. <https://doi.org/10.1029/2007JB005372>
- Gamero-Diaz, H., Miller, C. K., & Lewis, R. (2013). sCore: A mineralogy based classification scheme for organic mudstones. In *SPE Annual Technical Conference and Exhibition* (SPE-166284-MS). New Orleans: Society of Petroleum Engineers.
- Giorgetti, C., Carpenter, B. M., & Collettini, C. (2015). Frictional behavior of talc-calcite mixtures. *Journal of Geophysical Research: Solid Earth*, *120*, 6614–6633. <https://doi.org/10.1002/2015JB011970>
- Guglielmi, Y., Cappa, F., Avouac, J.-P., Henry, P., & Elsworth, D. (2015). Seismicity triggered by fluid injection-induced aseismic slip. *Sciences*, *348*(6240), 1224–1226. <https://doi.org/10.1126/science.aab0476>
- Guglielmi, Y., Elsworth, D., Cappa, F., Henry, P., Gout, C., Dick, P., & Durand, J. (2015). In situ observations on the coupling between hydraulic diffusivity and displacements during fault reactivation in shales. *Journal of Geophysical Research: Solid Earth*, *120*, 7729–7748. <https://doi.org/10.1002/2015JB012158>
- Ikari, M. J., Marone, C., & Saffer, D. M. (2011). On the relation between fault strength and frictional stability. *Geology*, *39*(1), 83–86. <https://doi.org/10.1130/g31416.1>
- Ikari, M. J., Niemeijer, A. R., & Marone, C. (2015). Experimental investigation of incipient shear failure in foliated rock. *Journal of Structural Geology*, *77*, 82–91. <https://doi.org/10.1016/j.jsg.2015.05.012>
- Im, K., Elsworth, D., & Fang, Y. (2018). The influence of preslip sealing on the permeability evolution of fractures and faults. *Geophysical Research Letters*, *45*, 166–175. <https://doi.org/10.1002/2017GRL076216>
- Jia, Y., Lu, Y., Elsworth, D., Fang, Y., & Tang, J. (2018). Surface characteristics and permeability enhancement of shale fractures due to water and supercritical carbon dioxide fracturing. *Journal of Petroleum Science and Engineering*, *165*, 284–297. <https://doi.org/10.1029/JB081i005p00881>
- Johnson, T. L., & Scholz, C. H. (1976). Dynamic properties of stick-slip friction of rock. *Journal of Geophysical Research*, *81*(5), 881–888. <https://doi.org/10.1029/JB081i005p00881>
- Keller, L. M. (2016). Porosity anisotropy of Opalinus Clay: implications for the poroelastic behaviour. *Geophysical Journal International*, *208*(3), 1443–1448.
- Kerrick, R. (1986). Fluid infiltration into fault zones: Chemical, isotopic, and mechanical effects. *Pure and Applied Geophysics*, *124*(1–2), 225–268. <https://doi.org/10.1007/BF00875727>
- Kilgore, B., Lozos, J., Beeler, N., & Oglesby, D. (2012). Laboratory observations of fault strength in response to changes in normal stress. *Journal of Applied Mechanics*, *79*(3), 031007. <https://doi.org/10.1115/1.4005883>

- Kohli, A. H., & Zoback, M. D. (2013). Frictional properties of shale reservoir rocks. *Journal of Geophysical Research: Earth Surface*, *118*, 5109–5125. <https://doi.org/10.1002/Jgrb.50346>
- Lin, A., Tanaka, N., Uda, S., & Satish-Kumar, M. (2003). Repeated coseismic infiltration of meteoric and seawater into deep fault zones: A case study of the Nojima fault zone, Japan. *Chemical Geology*, *202*(1-2), 139–153. <https://doi.org/10.1016/j.chemgeo.2003.08.010>
- Marone, C. (1995). Fault zone strength and failure criteria. *Geophysical Research Letters*, *22*(6), 723–726. <https://doi.org/10.1029/95GL00268>
- Marone, C. (1997). On the rate of frictional healing and the constitutive law for time- and slip-dependent friction. *International Journal of Rock Mechanics and Mining Science and Geomechanics Abstracts*, *34*(3-4), 347. [https://doi.org/10.1016/S1365-1609\(97\)00054-3](https://doi.org/10.1016/S1365-1609(97)00054-3)
- Moore, D. E., & Lockner, D. A. (2011). Frictional strengths of talc-serpentine and talc-quartz mixtures. *Journal of Geophysical Research*, *116*, B01403. <https://doi.org/10.1029/2010JB007881>
- Niemeijer, A., & Collettini, C. (2013). Frictional properties of a low-angle normal fault under in situ conditions: Thermally-activated velocity weakening. *Pure and Applied Geophysics*, *171*(10), 2641–2664. <https://doi.org/10.1007/s00024-013-0759-6>
- Niemeijer, A. R., & Spiers, C. J. (2007). A microphysical model for strong velocity weakening in phyllosilicate-bearing fault gouges. *Journal of Geophysical Research*, *112*, B10405. <https://doi.org/10.1029/2007JB005008>
- Nogues, J. P., Fitts, J. P., Celia, M. A., & Peters, C. A. (2013). Permeability evolution due to dissolution and precipitation of carbonates using reactive transport modeling in pore networks. *Water Resources Research*, *49*, 6006–6021. <https://doi.org/10.1002/wrcr.20486>
- Numelin, T., Marone, C., & Kirby, E. (2007). Frictional properties of natural fault gouge from a low-angle normal fault, Panamint Valley, California. *Tectonics*, *26*, TC2004. <https://doi.org/10.1029/2005TC001916>
- Ruina, A. (1983). Slip instability and state variable friction laws. *Journal of Geophysical Research*, *88*(B12), 10,359–10,370. <https://doi.org/10.1029/JB088iB12p10359>
- Rutter, E. H., & Mecklenburgh, J. (2017). Hydraulic conductivity of bedding-parallel cracks in shale as a function of shear and normal stress. *Geological Society, London, Special Publications*, *454*(1), 67–84. <https://doi.org/10.1144/SP454.9>
- Samuelson, J., & Spiers, C. J. (2012). Fault friction and slip stability not affected by CO₂ storage: Evidence from short-term laboratory experiments on North Sea reservoir sandstones and caprocks. *International Journal of Greenhouse Gas Control*, *11*(SUPPL), S78–S90. <https://doi.org/10.1016/j.ijggc.2012.09.018>
- Scholz, C. H. (1998). Earthquakes and friction laws. *Nature*, *391*(6662), 37–42. <https://doi.org/10.1038/34097>
- Scuderi, M. M., Niemeijer, A. R., Collettini, C., & Marone, C. (2013). Frictional properties and slip stability of active faults within carbonate–evaporite sequences: The role of dolomite and anhydrite. *Earth and Planetary Science Letters*, *369*, 220–232.
- Smith, S. A. F., & Faulkner, D. R. (2010). Laboratory measurements of the frictional properties of the Zuccale low-angle normal fault, Elba Island, Italy. *Journal of Geophysical Research*, *115*, B02407. <https://doi.org/10.1029/2008JB006274>
- Stesky, R. M., Brace, W. F., Riley, D. K., & Robin, P. Y. F. (1974). Friction in faulted rock at high temperature and pressure. *Tectonophysics*, *23*(1–2), 177–203. [https://doi.org/10.1016/0040-1951\(74\)90119-X](https://doi.org/10.1016/0040-1951(74)90119-X)
- Tesei, T., Collettini, C., Barchi, M. R., Carpenter, B. M., & Di Stefano, G. (2014). Heterogeneous strength and fault zone complexity of carbonate-bearing thrusts with possible implications for seismicity. *Earth and Planetary Science Letters*, *408*, 307–318. <https://doi.org/10.1016/j.epsl.2014.10.021>
- Verberne, B. A., He, C., & Spiers, C. J. (2010). Frictional properties of sedimentary rocks and natural fault gouge from the Longmen Shan fault zone, Sichuan, China. *Bulletin of the Seismological Society of America*, *100*(5B), 2767–2790. <https://doi.org/10.1785/0120090287>
- Verberne, B. A., Spiers, C. J., Niemeijer, A. R., De Bresser, J. H. P., De Winter, D. A. M., & Plümpner, O. (2014). Frictional properties and microstructure of calcite-rich fault gouges sheared at sub-seismic sliding velocities. *Pure and Applied Geophysics*, *171*(10), 2617–2640. <https://doi.org/10.1007/s00024-013-0760-0>
- Viti, C., Collettini, C., & Tesei, T. (2014). Pressure solution seams in carbonatic fault rocks: Mineralogy, micro/nanostructures and deformation mechanism. *Contributions to Mineralogy and Petrology*, *167*(2), 970. <https://doi.org/10.1007/s00410-014-0970-1>
- Wang, C., Elsworth, D., & Fang, Y. (2017). Influence of weakening minerals on ensemble strength and slip stability of faults. *Journal of Geophysical Research: Solid Earth*, *122*, 7090–7110. <https://doi.org/10.1002/2016JB013687>
- Wang, J., Jung, W., Li, Y., & Ghassemi, A. (2016). Geomechanical characterization of Newberry Tuff. *Geothermics*, *63*, 74–96.
- Xu, T., Rose, P., Fayer, S., & Pruess, K. (2009). On modeling of chemical stimulation of an enhanced geothermal system using a high pH solution with chelating agent. *Geofluids*, *9*(2), 167–177.
- Yildirim, L. T. O. (2014). Evaluation of petrophysical properties of gas shale and their change due to interaction with water (MS thesis). The Pennsylvania State University.
- Zoback, M. D., Kohli, A., Das, I., & McClure, M. (2012). The importance of slow slip on faults during hydraulic fracturing stimulation of shale gas reservoirs, SPE 155476. <https://doi.org/10.2118/155476-MS>